



A general strategy to synthesize single-atom metal-oxygen doped polymeric carbon nitride with highly enhanced photocatalytic water splitting activity

Fei Yu^a, Quanhua Deng^{a,b}, Haiping Li^{a,*}, Yuguo Xia^a, Wanguo Hou^a

^a National Engineering Research Center for Colloidal Materials, School of Chemistry and Chemical Engineering, Shandong University, Jinan, Shandong 250100, China

^b Stanley fertilizer (plain) Co., Ltd, Dezhou, Shandong 250100, China

ARTICLE INFO

Keywords:

Photocatalysis
Water splitting
Oxygen evolution
Carbon nitride
Single atom

ABSTRACT

Polymeric carbon nitride (PCN) is a prospective photocatalyst in water splitting to produce H₂, but its overall water splitting (OWS) activity is suppressed by the sluggish oxygen evolution reaction (OER). Herein, a general strategy involving electrostatic adsorption of oxometallate anions on protonated amorphous melon was proposed to synthesize single-atom metal-oxygen doped PCN (MO-PCN). MO-PCN exhibits highly enhanced photocatalytic OER and thereby OWS activity, benefitting from the MO structure functioning as OER active centers and enhancing photoexcited charge separation by introducing hole-trapping doping levels in bandgaps. This work provides a universal strategy to enhance OER activity of PCN-based photocatalysts.

1. Introduction

Continuous and increasing fossil fuel consumption has led to severe environmental and ecological deterioration, as well as impending energy deficiency [1,2]. Solar energy-driven photocatalytic water splitting to produce hydrogen, a clean fuel, has been considered a promising technology to cope with current environmental and energy issues [3]. Among the photocatalytic water splitting reactions, photocatalysts play the key role, and one of the most extensively researched photocatalysts with high potential for practical application is polymeric carbon nitride (PCN) discovered as a photocatalyst in 2009 [4], profiting from its advantages of low cost, non-toxicity, visible-light response, relatively high chemical stability, and appropriate energy band levels for the hydrogen evolution reaction (HER) and the oxygen evolution reaction (OER) [5]. However, the photocatalytic overall water splitting (OWS) activity of PCN is too low to meet the request for practical application (with the solar to hydrogen conversion efficiency (STH) reaching ~5–10% [6]), owing to its intrinsic defects including the low interfacial OER rate and low photoexcited charge separation and optical absorption capability [7,8].

Because of the sluggish interfacial OER of PCN, photocatalytic water splitting on PCN-based photocatalysts have been researched mainly around the HER in the presence of sacrificial agents [7], which is useful for property probe of photocatalysts but is almost meaningless to practical application, while the practicable photocatalytic OWS [9] was

much less researched. To enhance the interfacial OER rate of PCN, several means have been put forward, mainly including loading of co-catalysts (e.g., CoO_x, MnO_x, CoP, CoPi, RhO_x, IrO₂, RuO_x, PtO_x, CoAl₂O₄, and Co(OH)₂ [10–16]), carbon modification [17,18], and doping of single atoms (e.g., B, Mn, and Co [19–21]). For example, Zhao et al. synthesized B doped PCN with the apparent quantum yield (AQY) of OER at 380 nm reaching 3.7% [21] and then the B doped PCN ultrathin nanosheets were used to construct Z-scheme heterojunction for OWS with the STH reaching 1.2% [22]. Comparatively, cocatalyst loading can only increase the OER rates of PCN to a limited degree. Ways of carbon modification are finite. Single-atom doping shows higher application potential because there are many types of single atoms, especially single metal atoms capable of doping in PCN and the inserted single metal atoms may function as OER active sites [19,23] to considerably increase the interfacial OER rates. One convincing evidence suggesting the efficacy of single metal atom doping in enhancing photocatalytic activity is a series of Teixeira and coauthors' work in which many crystalline CN containing single metal atoms were synthesized via a simple ion exchange strategy [24–26].

To enhance the photoexcited charge separation and photoabsorption capability of PCN, a series of strategies were also successively proposed, such as tuning of morphologies [27], construction of heterojunction with narrow bandgap semiconductors [28], loading of noble metals [29], and structural modification [30] including organic group modification [31] and single atom doping [32,33]. In contrast, structural

* Correspondence to: 8364750.

E-mail address: hpli@sdu.edu.cn (H. Li).

<https://doi.org/10.1016/j.apcatb.2022.122180>

Received 25 August 2022; Received in revised form 2 November 2022; Accepted 12 November 2022

Available online 14 November 2022

0926-3373/© 2022 Elsevier B.V. All rights reserved.

modification is generally capable of narrowing the bandgap and introducing impurity levels in the bandgap of PCN to simultaneously enhance the optical absorption and photoexcited charge separation [34,35]. Relative to organic group modification, single metal atom doping is superior, thanks to its being able to work as OER active sites [23], and deserves to be deeply researched.

Hitherto, single metal atom doping of PCN are mainly realized by direct ion adsorption on PCN or its intermediates with subsequent calcination, or by direct calcination of mixtures containing feedstocks or intermediates of PCN and metal salts [19,20,36]. In comparison, the first method is easier to form single atoms in PCN, but new ways need to be explored to enhance the single atom adsorption on PCN and thereby increase the single atom doping concentrations. Recently, we found mechanic ball milling could largely enhance the metal ion (Co^{2+} as an example) adsorption on PCN with negative Zeta potential and increased the single atom Co concentration in the product by ~ 37 times [23]. However, as for metal ions which can only stably exist as oxometallate anions (MO_x^{n-}) in water, general methods are still of lack to enhance their adsorption on PCN or its intermediates with negative Zeta potential. Besides, single atom Co–O doping was proved to enhance photoabsorption and charge separation and work as the OER active site in our previous work [23], and formation of Mn–OH was also considered significant for the OER [19]. Nonetheless, more single atom M–O doped PCN still need be synthesized to further confirm the role of M–O in the OER.

In this work, a general electrostatic interaction strategy was used to enhance adsorption of MO_x^{n-} (e.g., CrO_4^{2-} , MoO_4^{2-} , and WO_4^{2-}) on protonated amorphous melon and substantially increase the single atom M–O doping concentration in the product (MO-PCN). MO-PCN exhibits highly enhanced photocatalytic OER and thereby OWS activity, relative to bulk PCN and common $\text{Co}(\text{OH})_2$ modified PCN ($\text{PCN}/\text{Co}(\text{OH})_2$), which benefits from the doping of single atom M–O that works as the OER active site and introduces an doping level in the bandgap to enhance photoabsorption and photoexcited charge separation. This work provides a universal way to insert single atom M–O in PCN for OER activity enhancement.

2. Experimental section

2.1. Synthesis of intermediates of PCN (MT_c) and protonated MT_c (MT_cH)

MT_c was prepared via direct pyrolysis of urea. Simply, urea (20 g, 99%, Aladdin) was added in a corundum crucible with a lid, calcined at T_c °C ($T_c = 480, 500, 520$, or 540) in air for 2 h in a muffle furnace, with a ramp rate of 5°C min^{-1} , and then cooled naturally to room temperature. The obtained product was denoted as MT_c .

To synthesize MT_cH , MT_c (0.5 g) was dispersed in the HCl aqueous solution (1.5 M, 100 mL) by sonification for 5 min, followed by stirring for 6 h. The suspension was filtrated, with the collected solid dried at 60°C for 12 h. The final product was denoted as MT_cH .

2.2. Synthesis of bulk PCN (PCNT_c)

For synthesis of PCNT_c , M500H (0.5 g) was added in a corundum crucible with a lid, calcined at T_c °C ($T_c = 550, 600$, or 620) for 2 h, with a ramp rate of 5°C min^{-1} , in N_2 atmosphere (with a flow rate of 100 mL min^{-1}) in a tube furnace. After naturally cooled to room temperature, the product was washed with water and dried at 60°C for 12 h. The final product was denoted as PCNT_c .

2.3. Preparation of $\text{PCNT}_c/\text{Co}(\text{OH})_2$

The chemical deposition of $\text{Co}(\text{OH})_2$ (3 wt%) on PCNT_c was carried out according to a reported way [16]. Simply, PCNT_c (0.1 g) was dispersed in ultrapure water (0.5 mL) by sonification for 10 min and

then the $\text{Co}(\text{NO}_3)_2 \cdot 0.6\text{H}_2\text{O}$ (99.99%, Aladdin) solution (2 g L^{-1} (Co), $750\text{ }\mu\text{L}$) was added to the dispersion. After stirring for 20 min, the concentrated ammonia solution (28%, 0.1 mL) was slowly dropped to the dispersion under stirring and then the dispersion continued to be stirred for 30 min at 60°C . The green solid was collected by filtration, washed with water, and dried at 60°C for 12 h. The final product was denoted as $\text{PCNT}_c/\text{Co}(\text{OH})_2$.

2.4. Synthesis of MO-PCN (M-PCNT_c)

For synthesis of Cr- PCNT_c , M500H (0.5 g) was dispersed in the $(\text{NH}_4)_2\text{CrO}_4$ (99.0%, Aladdin) solution (0.5 M, 50 mL) by sonification for 10 min. After stirring for 1 h at 30°C , the solid was collected by filtration, washed with water (10 mL), and dried at 60°C for 12 h. Then, the gained solid (marked as M500H/Cr, 0.5 g) was added in a corundum crucible with a lid, calcined at T_c °C ($T_c = 580, 600, 620$, or 640) for 2 h, with a ramp rate of 5°C min^{-1} , in N_2 atmosphere (with a flow rate of 100 mL min^{-1}) in a tube furnace. After naturally cooled to room temperature, the product was washed with water and dried at 60°C for 12 h. The final product was denoted as Cr- PCNT_c .

For synthesis of Mo- PCNT_c , M500H (0.5 g) was dispersed in the $(\text{NH}_4)_2\text{MoO}_4$ (99.98%, Aladdin) solution (0.5 M, 50 mL) by sonification for 10 min. After stirring for 1 h at 30°C , the solid was collected by filtration, washed with water (10 mL), and dried at 60°C for 12 h. Then, the obtained solid (marked as M500H/Mo, 0.5 g) was added in a corundum crucible with a lid, calcined at T_c °C ($T_c = 510, 530$, or 550) for 2 h, with a ramp rate of 5°C min^{-1} , in N_2 atmosphere (with a flow rate of 100 mL min^{-1}) in a tube furnace. After naturally cooled to room temperature, the product was washed with water and dried at 60°C for 12 h. The final product was denoted as Mo- PCNT_c .

For synthesis of W- PCNT_c , M500H (0.5 g) was dispersed in the $\text{Na}_2\text{WO}_4 \cdot 0.2\text{H}_2\text{O}$ (99.5%, Aladdin) solution (0.5 M, 50 mL) by sonification for 10 min. After stirring for 1 h at 30°C , the solid was collected by filtration, washed with water (10 mL), and dried at 60°C for 12 h (with the obtained sample marked as M500H/W) or added in the HCl aqueous solution (1.0 M, 100 mL), followed by stirring for 1 h. The suspension was filtrated and washed with water to $\text{pH} = \sim 6 - 7$ and the collected solid was dried at 60°C for 12 h. Then, the dry solid (0.5 g) was added in a corundum crucible with a lid, calcined at T_c °C ($T_c = 580, 600$, or 620) for 2 h, with a ramp rate of 5°C min^{-1} , in N_2 atmosphere (with a flow rate of 100 mL min^{-1}) in a tube furnace. After naturally cooled to room temperature, the product was washed with water and dried at 60°C for 12 h. The final product was denoted as W- PCNT_c .

For comparison, M500 was similarly processed as M500H. The collected solid from the $(\text{NH}_4)_2\text{CrO}_4$, $(\text{NH}_4)_2\text{MoO}_4$, or Na_2WO_4 suspension was denoted as M500/Cr, M500/Mo, or M500/W. M500/Mo was then processed similarly as M500H/Mo at $T_c = 550$ to synthesize the product, denoted as $\text{Mo}_L\text{-PCN550}$.

2.5. Theoretical calculations

The Vienna Ab Initio Package (VASP) [37,38] was employed to perform all the density functional theory (DFT) calculations within the generalized gradient approximation (GGA) using the PBE [39] formulation. We chose the projected augmented wave (PAW) potentials [40, 41] to describe the ionic cores and took valence electrons into account using a plane wave basis set with a kinetic energy cutoff of 450 eV. Partial occupancies of the Kohn-Sham orbitals were allowed using the Gaussian smearing method and a width of 0.05 eV. The electronic energy was considered self-consistent when the energy change was smaller than 10^{-5} eV. A geometry optimization was considered convergent when the force change was smaller than 0.02 eV/\AA . Grimme's DFT-D3 methodology [42] was used to describe the dispersion interactions.

The one-dimension PCN unit cell, which comprises of 12 H, 24 C and 36 N atoms, was used for all the calculations. During structural optimizations, the Γ point in the Brillouin zone was used for k -point

sampling, and all atoms were allowed to relax.

The formation energy (E), considered as the adsorption energy (E_{ads}) of adsorbate A was defined as,

$$E = E_{\text{ads}} = E_{\text{A/surf}} - E_{\text{surf}} - E_{\text{A(g)}} \quad (1)$$

where $E_{\text{A/surf}}$, E_{surf} , and $E_{\text{A(g)}}$ are the energy of adsorbate A adsorbed on the surface, the energy of clean surface, and the energy of isolated A molecule in a cubic periodic box with a side length of 20 Å and a $1 \times 1 \times 1$ Monkhorst-Pack k -point grid for Brillouin zone sampling, respectively.

The Gibbs free energy (G) of a gas phase molecule or an adsorbate on the surface was calculated by the equation,

$$G = E_{\text{a}} + \text{ZPE} - TS \quad (2)$$

where E_{a} is the total energy, ZPE is the zero-point energy, T is the temperature in kelvin (298.15 K here), and S is the entropy.

2.6. Photocatalytic water splitting

All the photocatalytic water splitting tests were conducted on a CEL-SPH2N-D photoactivity-evaluation system (Ceaulight, China) with the reaction temperature controlled at 10 °C by a flow of cooling water. For the photocatalytic OER, the photocatalyst (50 mg) and La_2O_3 (0.2 g) were dispersed in the AgNO_3 aqueous solution (0.01 M, 80 mL) by sonification for 5 min. Then, the dispersion was evacuated under stirring and the O_2 evolution was started under illumination of a CEL-PF300-T8E Xe lamp (set as 200 W) equipped with an AM 1.5 G filter ($\sim 560 \text{ mW cm}^{-2}$, measured by a CEL-NP2000 optical power meter, Ceaulight). The produced O_2 was tested via an on-line gas chromatograph (GC-7920, Ceaulight) with a thermal conductivity detector (TCD), using ultrapure Ar as the carrier gas. To determine apparent quantum yields (AQYs) of the photocatalyst, the OER was performed under irradiation of monochromatic light which was derived by substituting a series of Thorlabs band-pass filters (420–480 nm, USA) for above AM 1.5 G filter. The AQY was calculated by the equation,

$$\text{AQY} = 4R_{\text{O}}/(E_{\text{i}} \cdot A/E_{\text{p}}) \times 100\% \quad (3)$$

where R_{O} , E_{p} , A , and E_{i} are the O_2 evolution rate (mol s^{-1}), the photon energy (J mol^{-1}), the irradiation area (cm^2), and the irradiation intensity (W cm^{-2} , minus the transmission light intensity), respectively.

For the photocatalytic HER, the photocatalyst (50 mg) was dispersed in the triethanolamine (99.5%, Aladdin) aqueous solution (10 vol%, 100 mL) with addition of the $\text{H}_2\text{PtCl}_6 \cdot 0.6 \text{ H}_2\text{O}$ (AR, Aladdin) solution (0.01 M, 775 μL). After the system was evacuated, the Pt cocatalyst (3 wt % of the photocatalyst) was in-situ photodeposited on the photocatalyst under illumination of the 200-W CEL-PF300-T8E Xe lamp ($\sim 740 \text{ mW cm}^{-2}$) for 1 h. After the system was evacuated again, the HER was started under illumination of the 200-W Xe lamp with a cutoff filter ($\lambda \geq 420 \text{ nm}$, $\sim 580 \text{ mW cm}^{-2}$). Generated hydrogen was on-line analyzed by the gas chromatograph. AQYs for the HER were determined by replacing the ultraviolet cut-off filter with a series of Thorlabs band pass filters (420–500 nm). The AQY was calculated by the equation,

$$\text{AQY} = 2R_{\text{H}}/(E_{\text{i}} \cdot A/E_{\text{p}}) \times 100\% \quad (4)$$

where R_{H} is the H_2 evolution rate (mol s^{-1}).

For photocatalytic OWS, the photocatalyst (50 mg) was dispersed in ultrapure water (80 mL), followed by addition of the H_2PtCl_6 solution (0.01 M) with volume of 517, 775, or 1033 μL . The system was evacuated and photodeposition of Pt (2, 3, or, 4 wt% of the photocatalyst) on the photocatalyst was completed under irradiation of the 200-W Xe lamp. Then, the suspension was evacuated again and illuminated by the 200-W Xe lamp equipped with the AM 1.5 G filter to start the OWS reaction. For the cyclic photocatalytic tests, the system was evacuated before every run. The solar-to-hydrogen conversion efficiency (STH) was calculated according to the equation,

$$\text{STH} = R_{\text{H}} \cdot \Delta G^0/(E_{\text{i}} \cdot A) \times 100\% \quad (5)$$

where ΔG^0 denotes the Gibbs free energy variation for the OWS reaction (237 kJ mol^{-1}) and E_{i} was tuned as $\sim 100 \text{ mW cm}^{-2}$ by equipping the Xe lamp with two light attenuation filters and an AM 1.5 G filter.

3. Results and discussion

3.1. Synthesis and structures of MO-PCN

Fig. 1a shows the synthetic procedure of MO-PCN. MT_c exhibits negative Zeta potentials, $\sim -9 \pm 2 \text{ mV}$ (Fig. 1), while the Zeta potentials of protonated MT_c (MT_cH) become positive, gradually increasing from M540H to M500H and hardly changing at $T_c < 500$ (Fig. 1b). Considering M500H possesses high positive Zeta potentials (+30 mV) and its polycondensation degree is less than MT_cH ($T_c < 500$) upon subsequent calcination (i.e., more against the aggregation of surface adsorbed single atoms), it was chosen to adsorb MO_x^{n-} (Fig. 1a). Transmission electron microscopy (TEM) images show M500H and M500 contain similar nanosheet stack and aggregation structures with rich pores (Fig. S1a and b), indicating protonation of M500 hardly changed its morphology. The Zeta potentials of M500H after adsorption of MO_x^{n-} (M500H/M) became negative, while those of M500 after adsorption of MO_x^{n-} (M500/M) changed little (Figs. S2 and 1b), indicating relatively massive adsorption of MO_x^{n-} on M500H. M500H/W exhibits similar morphology as M500H (Fig. S1b and c), suggesting adsorption of MO_x^{n-} hardly changed the morphology of M500H. For M500H with surface adsorbed $(\text{NH}_4)_n\text{MO}_x$ (e.g., $(\text{NH}_4)_2\text{MoO}_4$ and $(\text{NH}_4)_2\text{CrO}_4$), direct calcination can form MO-PCN, but for M500H with adsorbed Y_nMO_x ($\text{Y} \neq \text{NH}_4$, e.g., Na_2WO_4), Y_nMO_x should first be capable of being transformed into solid H_nMO_x before calcination to form MO-PCN (Fig. 1a). The formed MO-PCN (denoted as M-PCNT_c in detail) possesses negative Zeta potentials which are close to those of bulk PCNT_c (Fig. S3), just like reported PCN and structurally modified PCN [43,44]. For Cr-PCN620, Mo-PCN550, and W-PCN600, their calcination temperature was optimized according to the photocatalytic OER and HER activity (Fig. S4), and nothing remained after calcination of M500H/Mo at $T_c > 560$. M-PCNT_c and PCNT_c all comprise similar porous aggregates of stacked nanosheets (Figs. S5 and S6) as M500H/W (Fig. S1c), suggesting the calcination would not remarkably change the morphology of M500H/M.

X-ray photoelectron spectroscopy (XPS) was performed to verify successful doping of metal elements in M-PCNT_c. As shown in Fig. 2a, the Cr 2p core-level XPS spectrum of Cr-PCN620 shows two peaks at binding energy of 586.5 and 577.2 eV, corresponding to Cr 2p_{1/2} and 2p_{3/2}, respectively [45]. The Mo 3d core-level XPS spectrum of Mo-PCN550 shows two couples of peaks at 235.1 and 232.0 eV and 233.1 and 230.0 eV with each couple assigned to Mo 3d_{3/2} and 3d_{5/2}, respectively [46,47]. And the W 4f core-level XPS spectrum of W-PCN600 shows two peaks at 37.2 and 35.2 eV, corresponding to W 4f_{5/2} and 4f_{7/2}, respectively [48]. These suggest the doping of metal elements in the samples. The contents of Cr in Cr-PCN620, Mo in Mo-PCN550, and W in W-PCN600 were determined as 0.42, 0.92, and 0.41 wt%, respectively, by inductively coupled plasma-optical emission spectrometry (ICP-OES), further verifying the doing of these metal elements. The sample (Mo_L-PCN550) obtained by calcining M500/Mo contains much less Mo (only 0.050 wt%, determined by the ICP-OES) than Mo-PCN550, indicating the necessity of protonation of M500 to enhance the adsorption of MO_x^{n-} . For Mo-PCN550 with the highest metal content, two couples of peaks in the Mo 3d spectrum are assigned to Mo in two different chemical microenvironments (e.g., with different chemical valence), but for Cr-PCN620 and W-PCN600, their Cr 3d and W 4f peaks are too weak to differentiate the chemical microenvironment. Therefore, taking Mo-PCN550 as an example, compared with its Mo 3d spectrum, the sample before calcination (M500H/Mo) shows only one couple of peaks at binding energy of 235.4 and 232.3 eV, corresponding to 3d_{3/2} and 3d_{5/2} of Mo^{6+} [49], and this couple of peaks are positioned

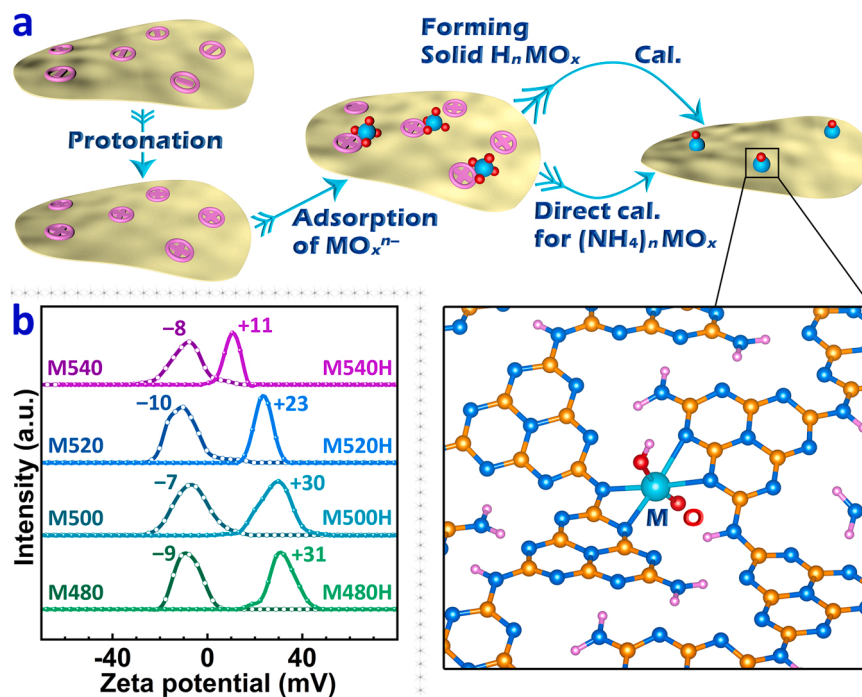


Fig. 1. (a) The simple synthetic procedure and framework structure of MO-PCN; and (b) Zeta potentials of MT_c and MT_cH ($\text{pH} = 6.25 \pm 0.10$).

0.4 and 2.4 eV higher than the two couples of Mo-PCN550, respectively, suggesting the probable reduction of Mo^{6+} , i.e. existence of Mo^{6-x} and Mo^{6-y} (e.g., Mo^V and Mo^{IV}) in Mo-PCN550.

O 1 s high-resolution XPS spectra of PCN620, PCN550, and PCN600 all show one peaks at binding energy of 532.0 eV (Fig. S7), ascribed to surface O–H [50]. The O 1 s spectra of Cr-PCN620, Mo-PCN550, and W-PCN600 also show one peaks, but at binding energy ~ 0.2 eV higher than those of corresponding PCNT_c, which probably results from formation of O–M bonds peaks of which are positioned on the right of [51, 52] but merged with the O–H peaks (Fig. S7). The calculated O/(C + N) molar ratios of M-PCNT_c from the XPS spectra (Table S1) and the calculated O content in M-PCNT_c from the elemental analysis and ICP-OES data (Table S2) are both greater than those of/in corresponding PCNT_c, further suggesting formation of O–M groups in M-PCNT_c. Besides, N/C molar ratios of M-PCNT_c and PCNT_c are not greater than the theoretical value (1.50), suggesting formation of nitrogen vacancies in the samples owing to secondary calcination in N_2 atmosphere [53], and gradually reduced N/C molar ratios from PCN550 to PCN620 (Table S2) indicate gradual increase of the nitrogen vacancies with increasing calcination temperature. Similar N/C molar ratios of M-PCNT_c and corresponding PCNT_c (Table S2) suggest similar nitrogen vacancy content in the samples. Fourier transform-infrared (FT-IR) spectra of M-PCNT_c and PCNT_c show similar absorption bands as reported PCN, i.e. those at 3630–2990, 1820–860, and 814 cm^{-1} ascribed to O–H/N–H stretching vibrations, C=N/C–N stretching vibrations, and the breathing mode of heptazine rings, respectively [23], indicative of similar basic framework structure of M-PCNT_c and corresponding PCNT_c, but O–H absorption bands of M-PCNT_c (3630–3440 cm^{-1}) are relatively stronger than those of corresponding PCNT_c (Fig. S8), suggesting the formation of M–OH in M-PCNT_c.

C 1 s high-resolution XPS spectra of M-PCNT_c and PCNT_c show four peaks, similarly as that of reported PCN (Fig. S9), e.g., the peaks of PCN600 at binding energy of 284.6, 286.1, 288.2, and 293.3 eV, assigned to adventitious carbon, $\pi-\pi^*$ of the adventitious carbon rings, N=C–N, and π excitation of heptazine rings, respectively [54,55]. Comparatively, the “N=C–N” peak of W-PCN600 shifts ~ 0.2 eV to the low binding energy (Fig. S9c), suggesting probable formation of (N=C–N)–W bonds the peak of which is positioned on the right of but

merged with the N=C–N peak. Owing to lower electron-donation capability of Cr and Mo than W, Cr-PCN620 and Mo-PCN550 exhibit similar “N=C–N” peaks as PCN620 and PCN550, respectively (Fig. S9a and b). N 1 s high-resolution XPS spectra of M-PCNT_c and PCNT_c also show four peaks similarly as reported PCN (Fig. S10), e.g., the peaks of PCN600 at 398.7, 400.0, 401.2, and 404.1 eV, assigned to C=N–C, N–H, N–C₃, and π excitation of the heptazine rings, respectively [54, 56]. In contrast, the “C=N–C, N–H, and N–C₃” peaks of W-PCN600 shift ~ 0.2 eV to the low binding energy (Fig. S10c), also suggesting probable formation of (N=C–N)–W bonds where the high electron-donation capability of W increases the electron density around the N atoms. Also because of the lower electron-donation capability of Cr and Mo, Cr-PCN620 and Mo-PCN550 exhibit similar peaks as PCN620 and PCN550, respectively (Fig. S10a and b). Overall, M-PCNT_c exhibits similar C 1 s and N 1 s spectra as corresponding PCNT_c, indicative of their similar framework structures, consistent with the FT-IR results. In addition, M-PCNT_c and PCNT_c exhibit similar X-ray diffraction (XRD) peaks as reported melon-type PCN with a layered orthorhombic structure [57–59], i.e. peaks at 13.3° and 27.3° corresponding to (210) and (002) crystal facets (Fig. S11), indicating their similar crystalline structures.

Energy dispersive X-ray spectroscopy (EDS) elemental mapping images of Mo-PCN550 (Fig. 2b) and W-PCN600 (Fig. 2c) show homogeneous distribution of Mo and W in the samples, respectively, further demonstrating the successful doping of metal elements in M-PCNT_c. To distinctly observe the dispersion state of metal elements in the samples, Cs-corrected high-angle annular dark-field scanning transmission electron microscopy (HAADF-STEM) was performed. As shown in Fig. 2d–g and S12, there are massive isolated bright dots in the high-resolution images of Mo-PCN550 and W-PCN600 (marked by dotted circles), which should be single Mo and W atoms, respectively. This effectively manifests the single-atom metal doping in M-PCNT_c.

To further confirm the single-atom metal doping structure in M-PCNT_c, taking Mo-PCN550 as an example, X-ray absorption spectroscopy was performed. Fig. 3a shows Mo K-edge X-ray absorption near-edge structure spectroscopy (XANES) spectra of Mo-PCN550, Mo foil, MoO_2 , and MoO_3 . The absorption-edge position of Mo-PCN550 approaches to that of MoO_2 (as shown by the arrow), with their peak

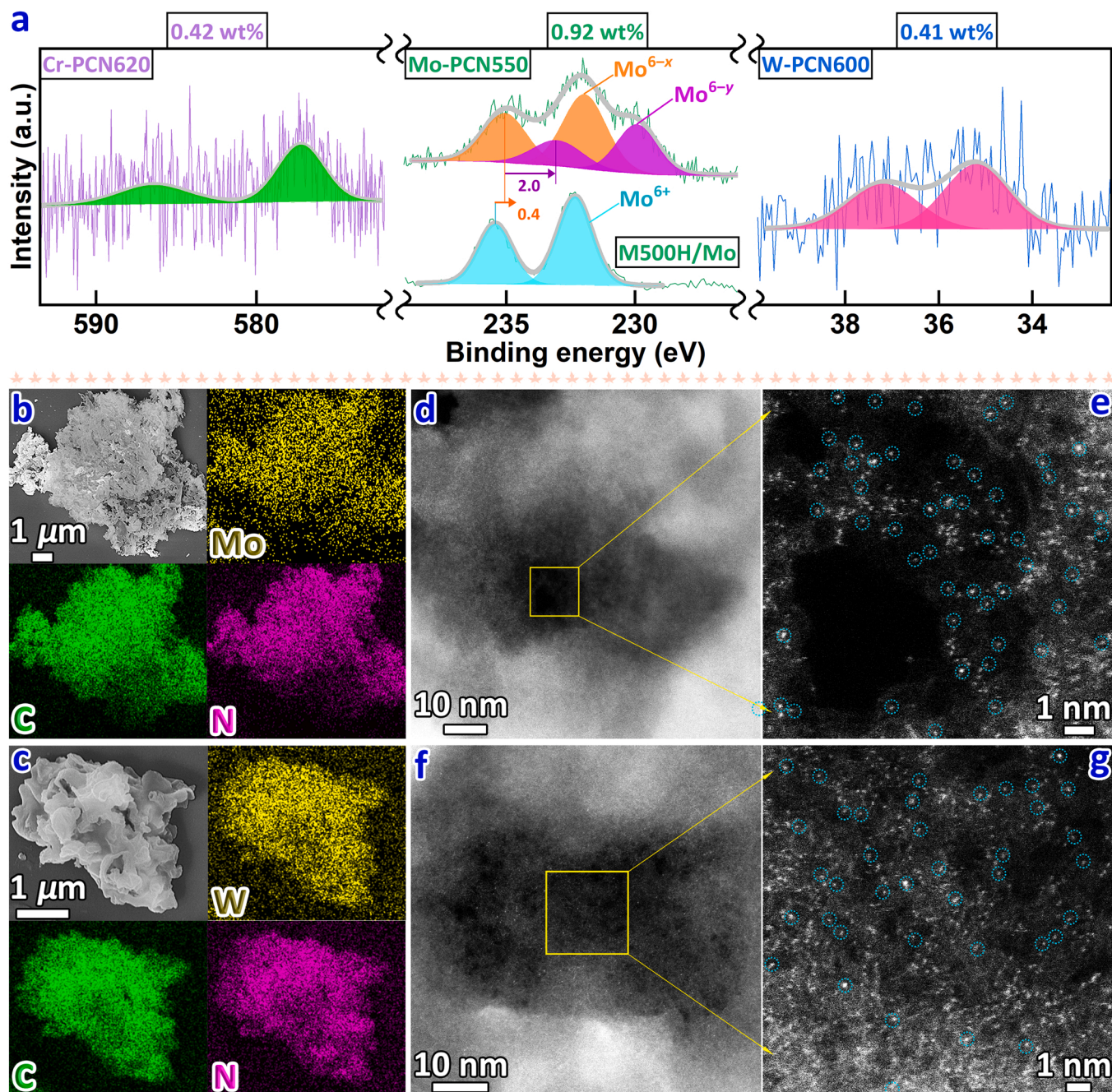


Fig. 2. (a) Cr 2p, Mo 3d, and W 4f core-level XPS spectra of Cr-PCN620, Mo-PCN550, and W-PCN600, respectively and metal element content in the samples determined by ICP-OES; (b, c) EDS elemental mapping images and (d, e, f, g) Cs-corrected HAADF-STEM images of (b, d, e) Mo-PCN550 and (c, f, g) W-PCN600.

positions also similar but far from those of Mo foil and MoO_3 (as shown by the vertical line), suggesting the mean valence of Mo in Mo-PCN550 is close to + 4. The chemical bonds around Mo were roughly determined by Fourier transformed k^2 -weighted extended X-ray absorption fine structure (EXAFS) analysis. As shown in Fig. 3b, a single Mo-ligand peak at 1.21 Å is observed in the spectrum of Mo-PCN550, different from the Mo-Mo coordination peak at 2.50 Å in the spectrum of Mo foil, the Mo-O peak at 1.57 Å and the Mo-Mo peaks at 2.18 and 3.31 Å in the spectrum of MoO_2 , and the Mo-O peaks at 1.10 and 1.61 Å and the Mo-Mo peak at 3.27 Å in the spectrum of MoO_3 , suggesting the single-atom dispersion of Mo atoms and probable formation of Mo-N/O bonds in Mo-PCN550. The wavelet transform contour plot of Mo-PCN550 shows only one intensity maximum at $k = 3.53 \text{ Å}^{-1}$ for the Mo-N/O (Fig. 3c), different from the plots of Mo foil (at $k = 8.27 \text{ Å}^{-1}$ for Mo-Mo,

Fig. 3d), MoO_2 (at $k = 5.70 \text{ Å}^{-1}$ for Mo-O and $k = 10.23 \text{ Å}^{-1}$ for Mo-Mo, Fig. 3e), and MoO_3 (at $k = 3.14 \text{ Å}^{-1}$ for Mo-O and $k = 9.77 \text{ Å}^{-1}$ for Mo-Mo, Fig. 3f), which further indicates the single-atom dispersion of Mo specie in Mo-PCN550 and the difference of the Mo-ligand structure in the sample from those in the others.

Least-square EXAFS curve fitting was carried out to confirm the Mo-N/O structure in Mo-PCN550, as shown in Fig. S13 and Tables S3 and S4. According to the PCN monolayer structure (Fig. S14) [60], the probable Mo-N/O structures are listed in Table S4. According to the single-shell or double-shell fitting results, only Mo-N₃O₂ and Mo-N₄O₂ are reasonable structures and their fitting curves are shown in Fig. S15.

Considering the valance of Mo close to + 4 and the structural stability (impossible for two OH connecting with Mo at 550 °C), the likely Mo-N₃O₂ and Mo-N₄O₂ structures include $\text{Mo}^{\text{V}}\text{-N}_3\text{OOH}$, $\text{Mo}^{\text{IV}}\text{-N}_4\text{OOH}$,

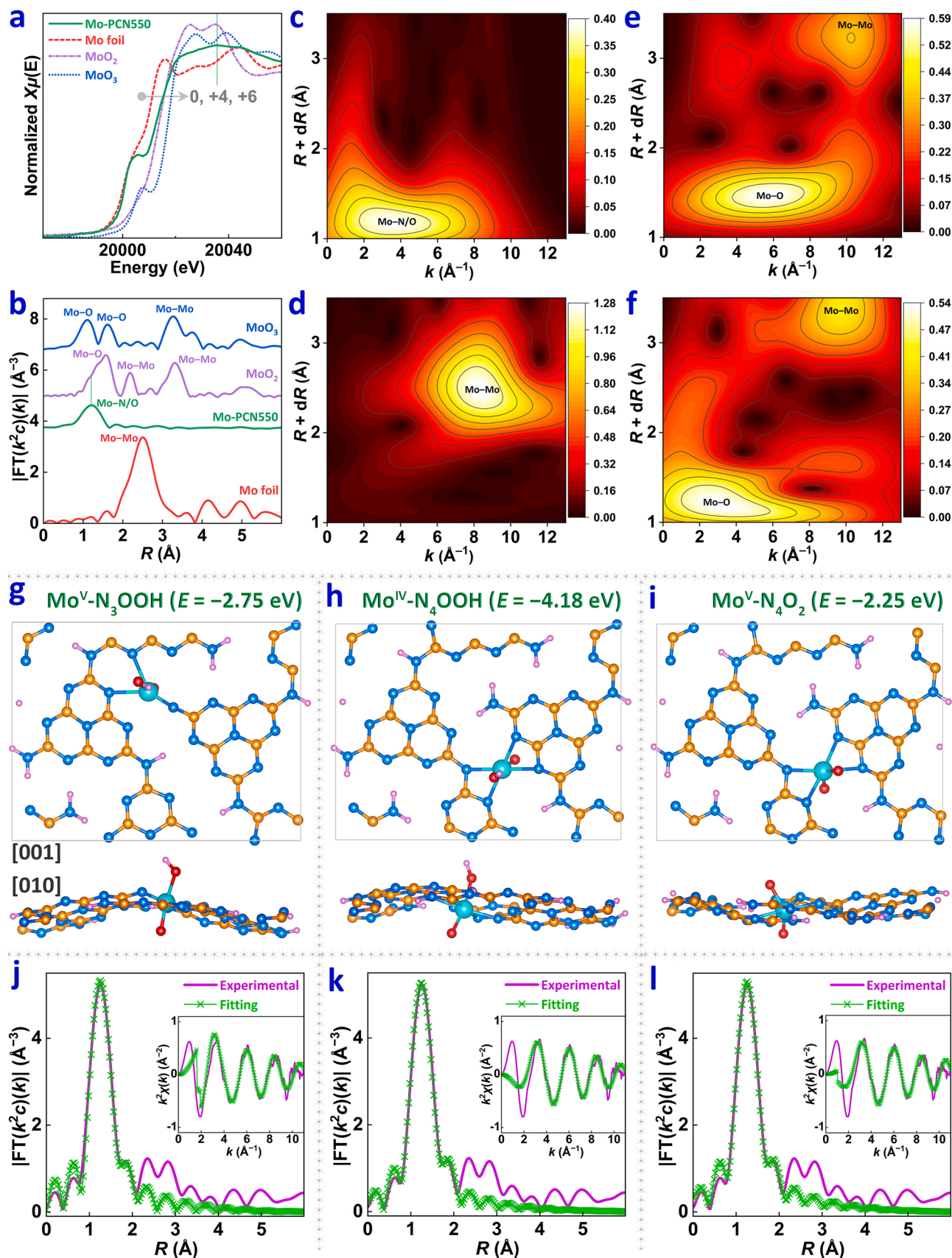


Fig. 3. Mo K-edge (a) XANES and (b) EXAFS spectra of Mo foil, MoO_2 , MoO_3 , and Mo-PCN550; wavelet transform contour plots of (c) Mo-PCN550, (d) Mo foil, (e) MoO_2 , and (f) MoO_3 ; (g–i) optimized structures of Mo-PCN550 with different doping configurations and their calculated formation energy (E); (j–l) R space- and (insets) k space-fitting curves of Mo-PCN550 with doping configurations in (g–i), respectively.

and $\text{Mo}^{\text{V}}\text{-N}_4\text{O}_2$. Their structural models optimized via density functional theory (DFT) calculations are shown in Fig. 3g–i. Apparently, two O atoms lie separately at two sides of the monolayers for each model. Based on these models, EXAFS curve fitting of Mo-PCN550 were performed. As shown in Fig. 3j–l and Table S5, the experimental and fitting curves match very well, and *R*-factors of the models are close (0.0080–0.0117), suggesting they are all possible structures in Mo-PCN550. However, the FT-IR spectra manifest formation of the Mo–OH and the valance of Mo approaches to +4, which indicates $\text{Mo}^{\text{IV}}\text{-N}_4\text{OOH}$ with mean Mo–N and Mo–O bond lengths of 1.98 and 1.72 Å, respectively (Table S5), is the main doping structure in Mo-PCN550, and suggests Mo^{6-x} and Mo^{6-y} in Fig. 2a are Mo^{V} and Mo^{IV} , respectively. The Mo^{V} likely belongs to surface $\text{Mo}^{\text{V}}\text{-N}_4\text{O}_2$ formed by oxidation of a few surface $\text{Mo}^{\text{IV}}\text{-N}_4\text{OOH}$ groups.

To further confirm rationality of the proposed Mo–N/O structures in Mo-PCN550, DFT calculations were conducted to acquire structural formation energy. As shown in Fig. 3g–i and Table S6, the formation energy of $\text{Mo}^{\text{IV}}\text{-N}_4\text{OOH}$ (−4.18 eV) is much less than that of $\text{Mo}^{\text{V}}\text{-N}_3\text{OOH}$ and $\text{Mo}^{\text{V}}\text{-N}_4\text{O}_2$ (−2.75 and −2.25 eV), demonstrating $\text{Mo}^{\text{IV}}\text{-N}_4\text{OOH}$ is the most probably formed structure in Mo-PCN550, consistent with the experimental results.

Nitrogen adsorption-desorption isotherms indicate M-PCNT_c and PCNT_c contain rich mesopores (Fig. S16). Mo-PCN550 exhibits higher specific surface area and pore volume ($77.5 \text{ m}^2 \text{ g}^{-1}$ and $0.338 \text{ cm}^3 \text{ g}^{-1}$)

than W-PCN600 ($39.0 \text{ m}^2 \text{ g}^{-1}$ and $0.167 \text{ cm}^3 \text{ g}^{-1}$) and PCN550 ($36.9 \text{ m}^2 \text{ g}^{-1}$ and $0.171 \text{ cm}^3 \text{ g}^{-1}$), but the surface area and pore volume of W-PCN600 and PCN600 are similar (Fig. S16), suggesting the single-atom metal type affects the mesoporous structure of the M-PCNT_c.

3.2. Energy band levels and photoexcited charge separation

Optical absorption capability of M-PCNT_c and PCNT_c were evaluated by UV–vis diffuse reflectance spectroscopy (Fig. 4a). Visible light absorption of M-PCNT_c is higher than that PCNT_c, which should be ascribed to the single-atom M–O doping [23]. Mo-PCN550 exhibits higher photoabsorption than W-PCN600, maybe related to the more mesopores in the former than in the latter, which facilitates multiple reflection of incident light [61]. The remarkably higher photoabsorption of PCN600 than PCN550 at 440–570 nm suggests formation of more nitrogen vacancies in PCN600 [62]. Tauc plots, considering the samples as indirect bandgap semiconductors [63], show that bandgaps (E_g) of PCN550, PCN600, Mo-PCN550, and W-PCN600 are 2.61, 2.50, 2.52 and 2.50 eV, respectively (the inset in Fig. 4a). The smaller E_g of Mo-PCN550 than PCN550, indicates the significant influence of single-atom Mo–O doping, but E_g of W-PCN600 and PCN600 is close, maybe because their relatively high content of nitrogen vacancies influencing E_g , as suggested by much less E_g of PCN600 than PCN550, covers the influence of single-atom W–O doping. Fig. 4b shows electron paramagnetic

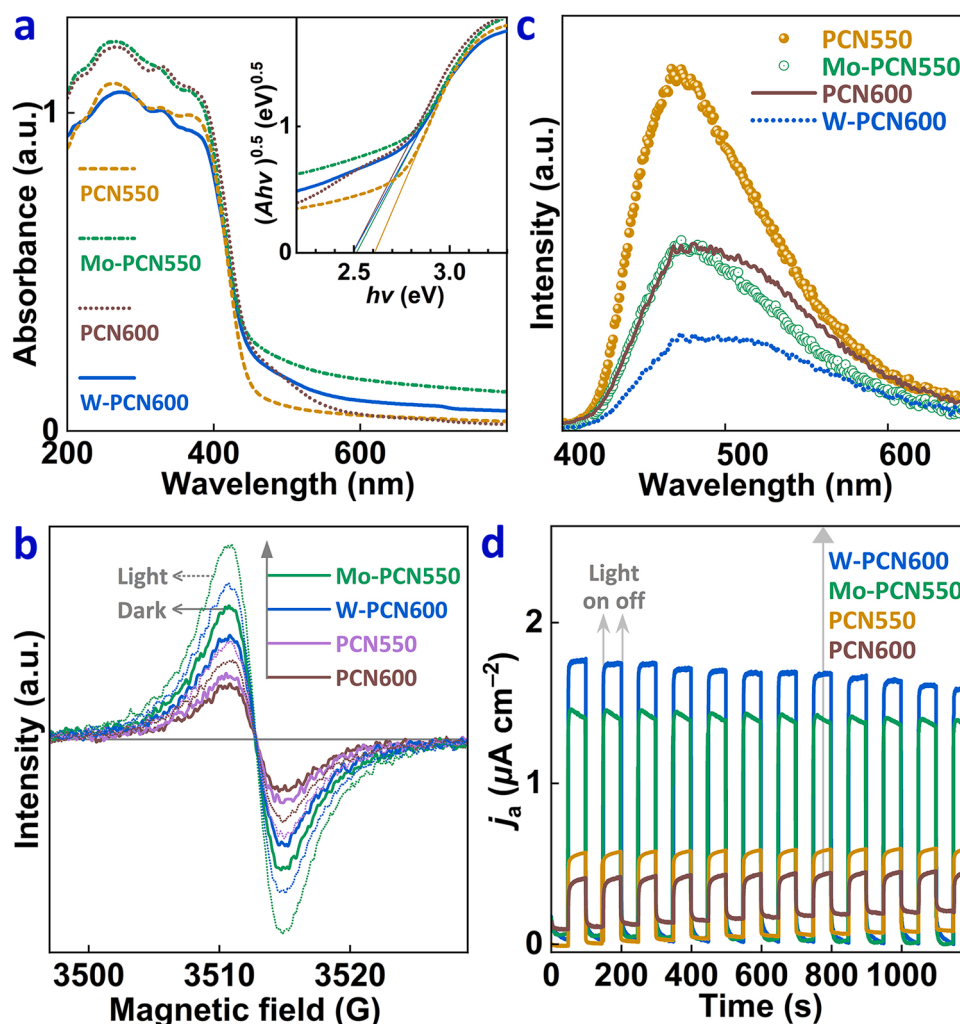


Fig. 4. (a) UV–vis diffuse reflectance spectra and (the inset) corresponding Tauc plots of W-PCN600, Mo-PCN550, PCN600, and PCN550; (b) EPR spectra of the samples in the dark and under light irradiation; (c) PL spectra of aqueous suspensions of samples (625 mg L^{-1}) containing MVCl_2 (1 mmol L^{-1}); and (d) anodic current density (j_a) of the samples under interval light irradiation.

resonance (EPR) spectra of the samples. All the spectra reveal single Lorentzian lines centered at g of 2.0039, ascribed to unpaired electrons in heptazine units [64]. In the dark, M-PCNT_c exhibits remarkably higher EPR signal intensity than PCNT_c, which mainly arises from the M–O doping that increases the delocalized electron density [23]. The relatively high signal intensity of Mo-PCN550, compared with that of W-PCN600, should result from the higher Mo–O content in the sample. Under visible light irradiation, the signal enhancement of M-PCNT_c is also higher than that of PCNT_c, suggesting that the M–O doping facilitates charge photoexcitation.

Given above results that increased photoabsorption and delocalized electron density enhance charge photoexcitation, photogenerated charge separation ability of the samples was further evaluated. As shown in Fig. 4c, M-PCNT_c exhibits considerably lower photoluminescence (PL) intensity than corresponding PCNT_c, in aqueous suspensions containing

methyl viologen dichloride (MVCl₂) that quenches electrons and inhibits surface charge recombination [64], indicative of suppressed bulk recombination of photogenerated charges by the single-atom M–O doping. In contrast, the PL spectra of W-PCN600 and PCN600 show more prominent shoulder peaks than those of Mo-PCN550 and PCN550, likely arising from more nitrogen vacancies in W-PCN600 and PCN600 [65,66], which also results in their relatively low PL intensity because the nitrogen vacancies can capture photogenerated electrons and suppress direct bulk recombination of charges [66]. In absence of MVCl₂, solid M-PCNT_c exhibits stronger PL intensity than solid PCNT_c (Fig. S17), likely owing to more serious surface recombination of charges [64]. Fig. 4d shows anodic photocurrent response of the samples. Apparently, the photocurrent density of M-PCNT_c is much higher than that of PCNT_c, indicating M–O doping can enhance photoexcited charge separation [23], consistent with the PL results. The higher

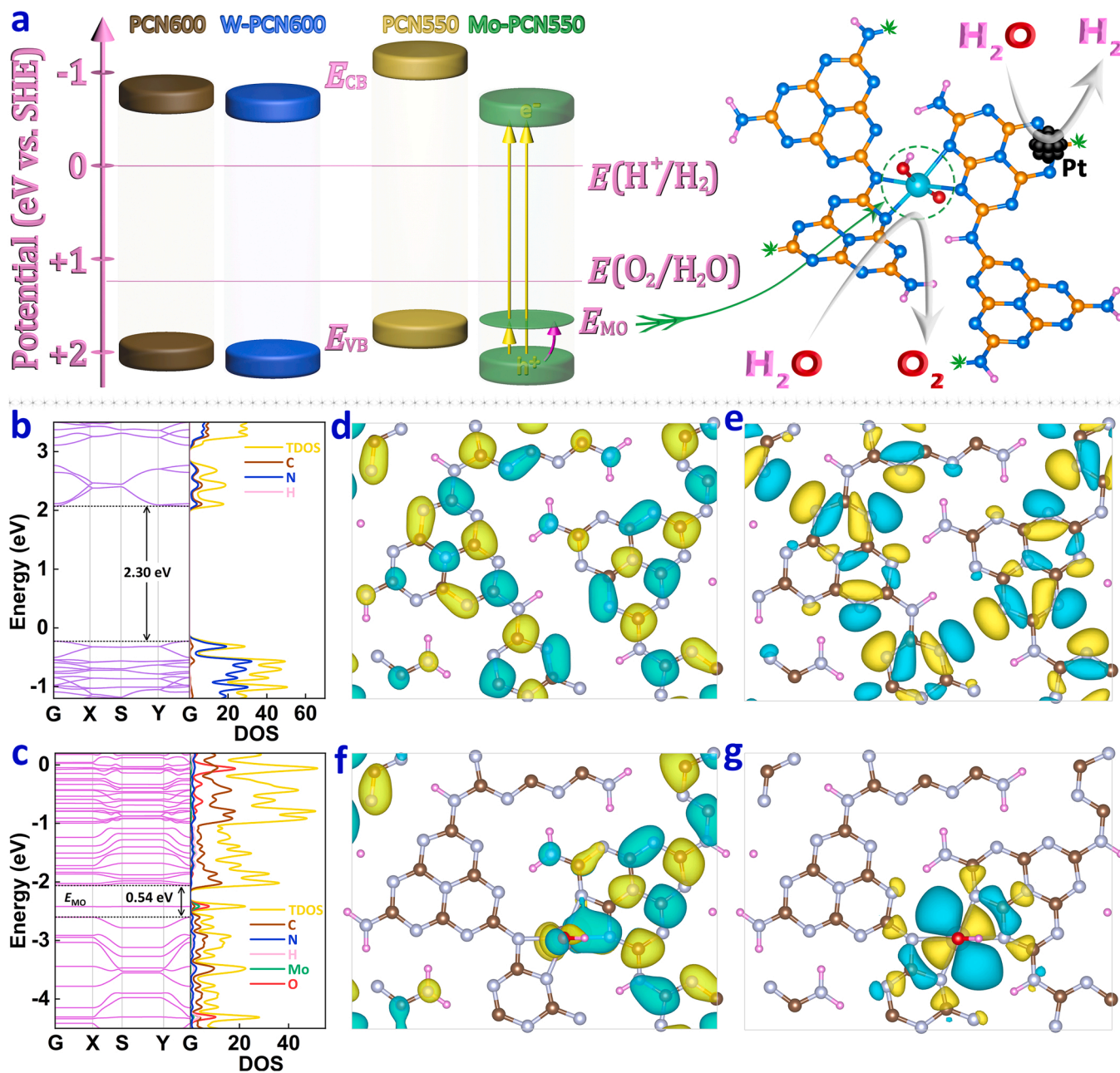


Fig. 5. (a) Energy band levels of samples and schematic illustration for the OER active center and the photocatalytic OWS process on Mo-PCN550; energy band and density of state (DOS) plots of (b) PCN and (c) Mo-PCN550 monolayers, obtained by DFT calculations; and corresponding (d, f) LUMO and (e, g) HOMO orbitals of (d, e) PCN and (f, g) Mo-PCN550 monolayers.

photocurrent density of W-PCN600 than Mo-PCN550 also reveals the efficacy of nitrogen vacancies.

To expound the function of M–O doping in enhancing the photoexcited charge separation, energy band levels of M-PCNT_c and PCNT_c were determined. Valance band (VB) edges (E_{VB}) of PCN600, W-PCN600, PCN550, and Mo-PCN550 were confirmed as 1.85, 1.94, 1.62, and 2.03 eV, respectively, by ultraviolet photoelectron spectroscopy (UPS) (Fig. S18). Then, their conduction band (CB) edges ($E_{CB} = E_{VB} - E_g$) are calculated as −0.65, −0.56, −0.99, and −0.49 eV, respectively. Energy band levels of the samples are shown in Fig. 5a. Apparently, the single-atom Mo–O doping lowers E_{CB} and E_{VB} . DFT calculations were conducted to further confirm the energy band levels, taking Mo-PCN550 as an example. As shown in Fig. 5b and c, the calculated E_g of Mo-PCN550 (0.54 eV) is much less than that of PCN (2.30 eV), and E_{CB} and E_{VB} of the former are much lower than those of the latter, in accordance with the experimental results. For PCN, the CB is contributed by C 2p and N 2p orbitals and the VB mainly by N2p orbitals, while for Mo-PCN550, both the CB and the VB are contributed by C 2p orbitals (Fig. 5b, 5c, and S19a–c), suggesting the significant effect of Mo–O doping on the VB. In addition, there is a prominent doping level (E_{MO}), close to E_{VB} , in the bandgap of Mo-PCN550, mainly contributed by O 2p and Mo 4p orbitals (Fig. 5b and S19d and e), further verifying the single-atom Mo–O doping effect. Similar calculation results have been reported for Co–OH and Pt–OH modified carbon nitride [23,67]. Given that the experimental Mo content (0.92 wt%) in Mo-PCN550 is much lower than that in the calculation model (10.29 wt%), practical E_{MO} in the bandgap may approach more to the VB. As shown in Fig. 5a, the E_{MO} can enhance photoabsorption and capture photogenerated holes to enhance the charge separation, which also suggests that M–O may function as the OER active center for photocatalytic water splitting. Besides, nitrogen vacancies may introduce a defect level, close to E_{CB} , in the bandgap which can enhance also photoabsorption and capture photoexcited electrons to enhance the charge separation [68,69], but is not the research emphasis in this work and not shown in Fig. 5a.

Fig. 5d and e shows the lowest unoccupied molecular orbital (LUMO) and the highest occupied molecular orbital (HOMO) locations of PCN. Apparently, the LUMO and HOMO orbits are uniformly delocalized in the heptazine units, owing to the high symmetry of the planar structure in the PCN framework. Comparatively, the charge density in Mo-PCN550 was redistributed with distinct electron-rich and electron-deficient regions formed, as shown by the LUMO and HOMO orbits in Fig. 5f and g. The localized charge accumulation may cause downshifting of E_{VB} and E_{CB} of PCN and formation of E_{MO} in the bandgap [21]. Especially, the spatial separation of electron-rich and electron-deficient regions would separate the redox sites, inhibiting the photoexcited

charge recombination [21]. The HOMO orbits of Mo-PCN550 are located around the Mo–O group, further suggesting the M–O functions as the OER active sites.

To further verify function of the M–O group or E_{MO} in trapping photogenerated holes (Fig. 5a), transient absorption (TA) spectroscopy was performed (Fig. S20). As shown in Fig. 6a and b, broad positive induced absorption features between 500 and 650 nm for Mo-PCN550 and PCN550 under 350-nm laser pulse excitation are attributed to overlapping electron and hole absorption [70]. Initial absorption (ΔA) of Mo-PCN550 is remarkably higher than that of PCN550, indicative of more charges generated in Mo-PCN550. To understand the charge transfer process, kinetic traces of the photogenerated charges were monitored at 635 nm (Fig. 6c). The decay curves of both Mo-PCN550 and PCN550 can be well fitted by a two-exponential model, as shown by solid lines in Fig. 6c. At early time scale, both curves show ultrafast rise of ΔA within 0.5 ps after 350-nm photoexcitation, indicative of instantaneous generation of charges. The fast decay within 100 ps (τ_1 , see the inset table in Fig. 6c) is related to direct recombination of photogenerated charges and charge transfer to trapping levels (delaying direct charge recombination) and the slow decay within several ns (τ_2) is ascribed to the recombination of trapped charges [71]. For PCN550, the τ_1 (35.3 ps) refers to electron transfer to the nitrogen vacancies, but for Mo-PCN550, the τ_1 (58.3 ps) refers to not only the electron transfer to the nitrogen vacancies but also the hole transfer to the E_{MO} (Fig. 5a), which makes τ_1 of Mo-PCN550 greater. The τ_2 (5.42 ns) of Mo-PCN550 is also much greater than that (1.67 ns) of PCN550, because the trapping of holes at the E_{MO} relatively delays the charge recombination. Overall, the M–O group can trap photogenerated holes to suppress recombination of charges and enhance their participation in water splitting.

3.3. Photocatalytic Water Splitting Activity and Related Mechanism

In view of the single-atom M–O functioning as the OER active center in M-PCNT_c, the photocatalytic OER activity of samples was firstly evaluated with AgNO₃ as the electron acceptor under irradiation of a Xe lamp with an AM 1.5 G filter (simulated solar light). As shown in Fig. 7a, PCNT_c exhibits no OER activity, but M-PCNT_c and PCNT_c/Co(OH)₂ exhibit oxygen evolution with time, indicating the photocatalytic process proceeds and the single-atom M–O groups indeed work as the OER active sites. Apparently, the OER activity of M-PCNT_c is higher than corresponding PCNT_c/Co(OH)₂. The average OER rates (R_O) in 7 h for W-PCN600, Mo-PCN550, and Cr-PCN620 (6.7, 5.2, and 2.4 $\mu\text{mol h}^{-1}$) are 7.4, 2.9, and 1.8 times higher than those of PCN600/Co(OH)₂, PCN550/Co(OH)₂, and PCN620/Co(OH)₂, respectively (Fig. 7b). The R_O in 1 h for W-PCN600 can reach 10.6 $\mu\text{mol h}^{-1}$. The gradual decrease of

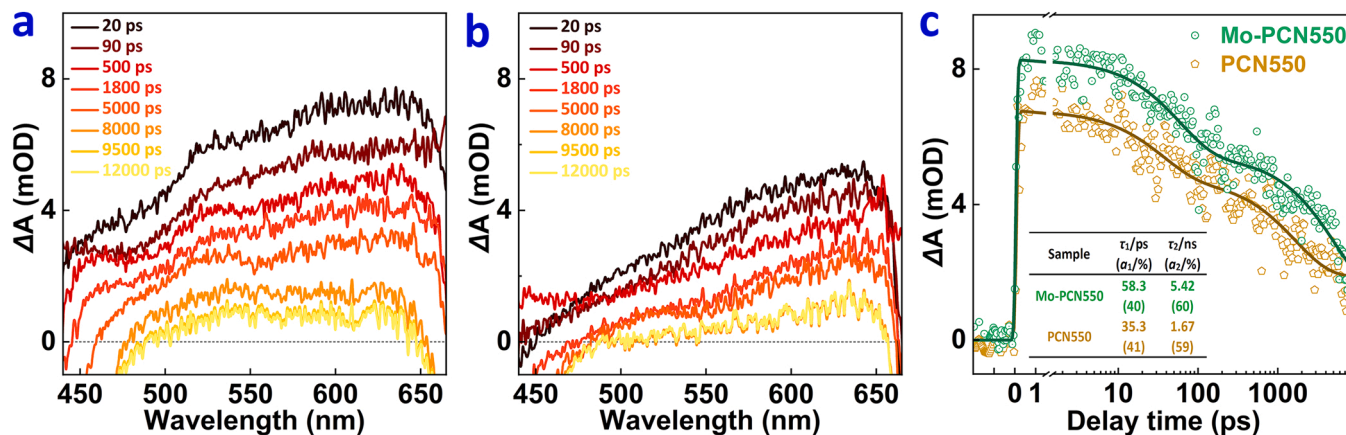


Fig. 6. TA spectra recorded at indicated delay times measured with 350-nm excitation for (a) Mo-PCN550 and (b) PCN550 and (c) corresponding TA kinetic traces of the samples at 635 nm within 9500 ps. Data in (c) are lifetimes (τ_1 and τ_2) and their percentages (a_1 and a_2) gained by fitting the curves using a two-exponential model.

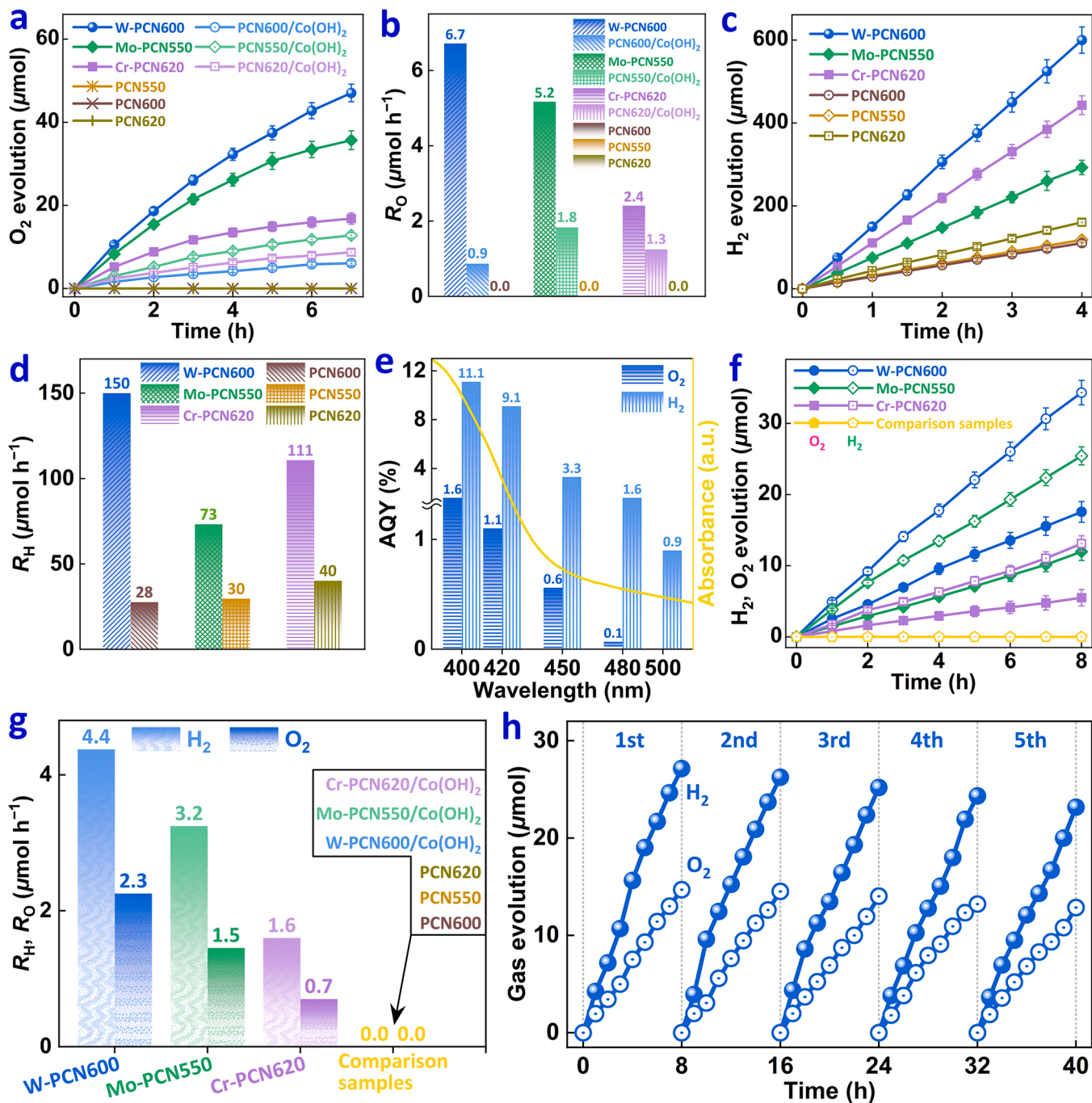


Fig. 7. (a) Photocatalytic oxygen evolution on various samples with AgNO_3 as the sacrificial agent under simulated solar light and (b) corresponding average OER rates (R_O) in 7 h; (c) photocatalytic hydrogen evolution on various samples with triethanolamine as the sacrificial agent under visible light ($\lambda \geq 420$ nm) irradiation and (d) corresponding HER rates (R_H); (e) apparent quantum yields (AQYs) of W-PCN600 under various monochromatic light for the OER in 1 h and the HER; (f) photocatalytic OWS under simulated solar light and (g) corresponding R_H and R_O for M-PCNT_c and comparison samples with 3 wt% Pt as the cocatalyst; and (h) the cyclic experiment of photocatalytic OWS on W-PCN600.

R_O with time results from the photodeposited Ag particles on the sample that cover the surface active sites [72]. Furthermore, the photocatalytic HER activity of the samples was assessed with triethanolamine as the electron donor under visible light ($\lambda \geq 420$ nm) irradiation. As shown in Fig. 7c, M-PCNT_c and PCNT_c all exhibit proceeding of the photocatalytic HER, and the activity of M-PCNT_c is higher than that of PCNT_c. The corresponding HER rates (R_H) of W-PCN600, Mo-PCN550, and Cr-PCN620 (150, 73, and 111 $\mu\text{mol h}^{-1}$) are 5.4, 2.4, and 2.8 times higher than those of PCN600, PCN550, and PCN620, respectively (Fig. 7d). Apparent quantum yields (AQYs) of OER and HER on

W-PCN600 under various monochromatic light are shown in Fig. 7e. The AQYs change well along with the UV-vis diffuse reflectance spectrum, suggesting the significant influence of photoabsorption capability. The AQYs for the OER in 1 h (Fig. S21) at 400, 420, 450, and 480 nm are 1.6%, 1.1%, 0.6%, and 0.1%, respectively, and those for the HER (Fig. S22) decrease from 11.1% at 400 nm to 0.9% at 500 nm. Compared with reported results, the photocatalytic OER performance of W-PCN600 is among the excellent (Table S7).

To unravel significance of the OER acceleration in enhancing photocatalytic OWS, the photocatalytic OWS activity of M-PCNT_c, PCNT_c,

and PCNT_c/Co(OH)₂ were evaluated with Pt as the cocatalyst under irradiation of simulated solar light. As shown in Fig. 7f, M-PCNT_c with 3 wt% Pt which is optimized according to the photocatalytic OWS rates of W-PCN600 loaded with different content of Pt (Fig. S23) exhibits linear increase of H₂ and O₂, revealing proceeding of the OWS process, but no produced gas was detected for comparison samples (PCNT_c and PCNT_c/Co(OH)₂) also containing 3 wt% Pt, which effectively indicates the pivotal role of the single-atom M–O doping in enhancing the photocatalytic OER and thereby OWS activity. Fig. 7g shows R_H and R_O of M-PCNT_c in photocatalytic OWS and their R_H/R_O ratios are close to 2:1, indicative of negligible side reactions. The OWS activity of M-PCNT_c follows the order, W-PCN600 > Mo-PCN550 > Cr-PCN620, with W-PCN600 exhibiting R_O and R_H of 2.3 and 4.4 $\mu\text{mol h}^{-1}$. This sequence is consistent with the sequence of OER activity (Fig. 7b), but inconsistent with that of HER activity (Fig. 7d), manifesting that the photocatalytic OWS activity of M-PCNT_c depends decisively on their interfacial OER rates. The AQY for OWS on W-PCN600 at 420 nm (Fig. S24) was determined as 0.017%, and the STH for the OWS on W-PCN600 under simulated solar light (set as $\sim 100 \text{ mW cm}^{-2}$) (Fig. S25) was calculated to be 0.006%. The photocatalytic OWS activity of M-PCNT_c is not higher than recently reported results of other photocatalysts, but it indeed reveals the necessity of expediting the OER to enhance the OWS activity. Overall, H₂ and O₂ can be continuously produced on M-PCNT_c, benefitting from the E_{MO} enhanced photogenerated charge separation and the single-atom M–O groups functioning as the OER active centers, though Pt functions as the active site for the backward reaction of OWS.

The surface area normalized photocatalytic OER rates of W-PCN600 ($3.4 \mu\text{mol h}^{-1} \text{m}^{-2}$) is still 6.8 times higher than that ($0.5 \mu\text{mol h}^{-1} \text{m}^{-2}$) of PCN600/Co(OH)₂ (considering Co(OH)₂ did not affect surface area of PCNT_c), which manifests the surface area is not a significant factor leading to the photoactivity enhancement. Visible light absorption of W-PCN600 is not much higher than that of PCN600, indicating the photoabsorption increase is not an important factor, either. The surface area normalized photocatalytic HER rates of W-PCN600 ($76.9 \mu\text{mol h}^{-1} \text{m}^{-2}$) is 5.5 times higher than those of PCN600 ($14.0 \mu\text{mol h}^{-1} \text{m}^{-2}$), which effectively demonstrates that the enhancement of photoexcited charge separation is a significant factor for improvement of the photoactivity. Certainly, the single-atom M–O group functioning as the OER active site is the key factor for enhancement of the OER and OWS activity.

Fig. 7h shows the cyclic photocatalytic OWS experiment of W-PCN600. After five-consecutive runs, the OWS rates decrease only $\sim 13\%$, indicating relatively high stability of the sample. The W 4f core-level XPS spectrum of W-PCN600 after the cyclic experiment (marked as W-PCN600-Af) shows similar one couple of peaks and its N 1s core-level spectrum shows similar three peaks as those of the pristine W-PCN600, respectively (Fig. S26a and b), indicating high structural stability of the sample in the OWS process, but the peak positions relatively shift, which likely results from the influence of surface photodeposited Pt, as revealed by the Pt 4f core-level XPS spectrum of W-PCN600-Af which shows two couples of peaks at binding energy of 75.9 and 72.5 eV and

74.7 and 71.3 eV (Fig. S26c), corresponding to Pt^{II}–O and Pt⁰ [73], respectively. The O 1s spectrum of W-PCN600-Af shows one peak at 531.8 eV (Fig. S26d), similarly as the pristine W-PCN600, assigned to O–W/O–H, as well as the other peak at 532.2 eV, corresponding to O–Pt^{II} [74], and the calculated (O–W/O–H)/(C + N) ratio of W-PCN600-Af (0.0166) is close to that of W-PCN600 (0.0157) (Table S1), which also suggests the high structural stability of W-PCN600.

Considering the decisive role of the interfacial OER rate in photocatalytic OWS, the OER mechanism based on the M–OH structure of MO-PCN was probed. As shown Fig. 8a, the OER process was proposed according to reported results of Mn doped PCN [19]. Four holes are needed to complete the OER process via four oxidation steps [75]. The M–OH structure may more facilitate the water oxidation, compared with M without OH coordination, by leaving out the initial adsorption of H₂O molecules [19] and recovering the structure synchronously with O₂ generation (Step 4).

The photocatalytic OER mechanism was further investigated by the calculated Gibbs free energy change (ΔG) diagrams, with optimized structural models of intermediates for MoO-PCN and WO-PCN also provided (Fig. 8b and S27). As shown in Fig. 8b, all the steps for MoO-PCN and WO-PCN are thermodynamically uphill. The theoretical results indicate that the OER on MoO-PCN and WO-PCN can proceed through the proposed four steps (Fig. 8a) with O–M–OOH as the key intermediates, i.e., Step 3 as the rate-determining steps. Apparently, the calculated ΔG for the rate-determining step at the MoO-PCN interface (2.60 eV) is lower than that at the WO-PCN interface (3.14 eV), manifesting MoO-PCN possesses higher interfacial water oxidation ability [76] than WO-PCN. Considering Mo-PCN550 also possesses larger surface area (Fig. S16a) and higher photoabsorption performance (Fig. 4a) than W-PCN600, the higher photocatalytic OER activity of W-PCN600 (Fig. 7b) should arise from its higher photoexcited charge separation efficiency that benefits from the higher ability of W-PCN600 in capturing photogenerated holes, as indicated by its much smaller ΔG for Step 1 (0.39 eV) than that of Mo-PCN550 (1.21 eV) (Fig. 8b), which also suggests the advantage of the M–OH structure in photocatalytic OER, and also from its higher ability in capturing photogenerated electrons because of containing more nitrogen vacancies.

4. Conclusions

A general strategy including protonation of amorphous melon and subsequent adsorption of MO_x^{n-} (e.g., WO_4^{2-} , MoO_4^{2-} , and CrO_4^{2-}) was proposed to synthesize MO-PCN. The protonation of amorphous melon could considerably enhance the adsorption of MO_x^{n-} by electrostatic interactions and thereby increase the single atom doping concentrations in MO-PCN. Taking MoO-PCN as an example, the single atom M–O doping structure was determined mainly as $\text{Mo}^{\text{IV}}\text{–N}_4\text{OOH}$ which functions as the OER active center, narrows the bandgap, introduces a doping level close to the VB edge in the bandgap to capture

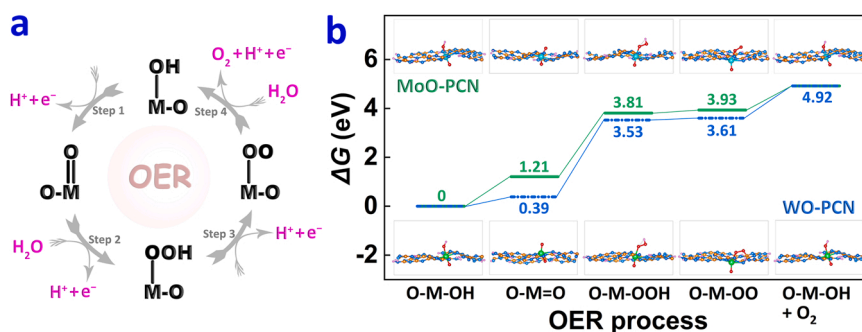


Fig. 8. (a) Schematic illustration for the OER process on MO-PCN; and (b) DFT calculation-obtained Gibbs free energy change (ΔG) and optimized structural models of intermediates for the OER on MoO-PCN and WO-PCN.

photogenerated holes and enhance the charge separation, and thus largely improve the photocatalytic OER, HER, and thereby OWS activity. WO-PCN exhibits the highest photocatalytic OER and OWS rates and its OER rate is ~ 7.4 times that of bulk PCN/Co(OH)₂, with the AQY at 400 nm reaching 1.6%. Benefitting from the higher photoexcited charge separation efficiency, WO-PCN exhibits higher photocatalytic activity than MoO-PCN, though MoO-PCN possesses the higher water oxidation ability. WO-PCN exhibits relatively high stability in photocatalytic OWS. Overall, this work provides a universal way to synthesize MO-PCN with high photocatalytic OER activity and may largely contribute to design of efficient photocatalysts in OWS.

CRedit authorship contribution statement

Fei Yu: Conceptualization, Methodology, Formal analysis, Writing - original draft. **Quanhua Deng:** Methodology, Investigation. **Haiping Li:** Conceptualization, Formal analysis, Writing - review & editing, Funding acquisition. **Yuguo Xia:** Methodology. **Wanguo Hou:** Funding acquisition, Writing - review & editing.

Declaration of Competing Interest

The authors declare that they have no known competing financial interests or personal relationships that could have appeared to influence the work reported in this paper.

Data Availability

Data will be made available on request.

Acknowledgments

This work was supported by the National Natural Science Foundation of China (No. 21872082) and the Young Scholars Program of Shandong University in China (No. 2018WLJH39). We are grateful for the assistance of Shandong University Structural Constituent and Physical Property Research Facilities (SDU SCPPRF) and Shiyanjia Lab (www.shiyanjia.com).

Appendix A. Supporting information

Supplementary data associated with this article can be found in the online version at [doi:10.1016/j.apcatb.2022.122180](https://doi.org/10.1016/j.apcatb.2022.122180).

References

- [1] S. Ezendam, M. Herran, L. Nan, C. Gruber, Y. Kang, F. Grobmeyer, R. Lin, J. Gargiulo, A. Sousa-Castillo, E. Cortes, Hybrid plasmonic nanomaterials for hydrogen generation and carbon dioxide reduction, *ACS Energy Lett.* 7 (2022) 778–815.
- [2] H. Lin, S. Luo, H. Zhang, J. Ye, Toward solar-driven carbon recycling, *Joule* 6 (2022) 294–314.
- [3] Y. Fang, Y. Hou, X. Fu, X. Wang, Semiconducting polymers for oxygen evolution reaction under light illumination, *Chem. Rev.* 122 (2022) 4204–4256.
- [4] X. Wang, K. Maeda, A. Thomas, K. Takanabe, G. Xin, J.M. Carlsson, K. Domen, M. Antonietti, A metal-free polymeric photocatalyst for hydrogen production from water under visible light, *Nat. Mater.* 8 (2009) 76–80.
- [5] Y. Wang, S.Z.F. Phua, G. Dong, X. Liu, B. He, Q. Zhai, Y. Li, C. Zheng, H. Quan, Z. Li, Y. Zhao, Structure tuning of polymeric carbon nitride for solar energy conversion: From nano to molecular scale, *Chem* 5 (2019) 2775–2813.
- [6] Y. Nishiyama, T. Yamada, M. Nakabayashi, Y. Maehara, M. Yamaguchi, Y. Kuromiya, Y. Nagatsuma, H. Tokudome, S. Akiyama, T. Watanabe, R. Narushima, S. Okunaka, N. Shibata, T. Takata, T. Hisatomi, K. Domen, Photocatalytic solar hydrogen production from water on a 100-m² scale, *Nature* 598 (2021) 304–307.
- [7] W.J. Ong, L.L. Tan, Y.H. Ng, S.T. Yong, S.P. Chai, Graphitic carbon nitride (g-C₃N₄)-based photocatalysts for artificial photosynthesis and environmental remediation: Are we a step closer to achieving sustainability? *Chem. Rev.* 116 (2016) 7159–7329.
- [8] G.Z.S. Ling, S.F. Ng, W.J. Ong, Tailor-engineered 2D cocatalysts: Harnessing electron-hole redox center of 2D g-C₃N₄ photocatalysts toward solar-to-chemical conversion and environmental purification, *Adv. Funct. Mater.* (2022), 2111875.
- [9] P. Niu, J. Dai, X. Zhi, Z. Xia, S. Wang, L. Li, Photocatalytic overall water splitting by graphitic carbon nitride, *InfoMat* 3 (2021) 931–961.
- [10] G. Zhang, Z.A. Lan, X. Wang, Surface engineering of graphitic carbon nitride polymers with cocatalysts for photocatalytic overall water splitting, *Chem. Sci.* 8 (2017) 5261–5274.
- [11] X. Chen, R. Shi, Q. Chen, Z. Zhang, W. Jiang, Y. Zhu, T. Zhang, Three-dimensional porous g-C₃N₄ for highly efficient photocatalytic overall water splitting, *Nano Energy* 59 (2019) 644–650.
- [12] Z. Pan, Y. Zheng, F. Guo, P. Niu, X. Wang, Decorating CoP and Pt nanoparticles on graphitic carbon nitride nanosheets to promote overall water splitting by conjugated polymers, *ChemSusChem* 10 (2017) 87–90.
- [13] L. Ge, C. Han, X. Xiao, L. Guo, In situ synthesis of cobalt-phosphate (Co-Pi) modified g-C₃N₄ photocatalysts with enhanced photocatalytic activities, *Appl. Catal. B* 142–143 (2013) 414–422.
- [14] F. Raziq, L. Sun, Y. Wang, X. Zhang, M. Humayun, S. Ali, L. Bai, Y. Qu, H. Yu, L. Jing, Synthesis of large surface-area g-C₃N₄ comodified with MnO₂ and Au-TiO₂ as efficient visible-light photocatalysts for fuel production, *Adv. Energy Mater.* 8 (2018), 1701580.
- [15] T. Kanazawa, K. Kato, R. Yamaguchi, T. Uchiyama, D. Lu, S. Nozawa, A. Yamakata, Y. Uchimoto, K. Maeda, Cobalt aluminate spinel as a cocatalyst for photocatalytic oxidation of water: significant hole-trapping effect, *ACS Catal.* 10 (2020) 4960–4966.
- [16] G. Zhang, S. Zang, X. Wang, Layered Co(OH)₂ deposited polymeric carbon nitrides for photocatalytic water oxidation, *ACS Catal.* 5 (2015) 941–947.
- [17] J. Liu, Y. Liu, N. Liu, Y. Han, X. Zhang, H. Huang, Y. Lifshitz, S.-T. Lee, J. Zhong, Z. Kang, Metal-free efficient photocatalyst for stable visible water splitting via a two-electron pathway, *Science* 347 (2015) 970–974.
- [18] W. Che, W. Cheng, T. Yao, F. Tang, W. Liu, H. Su, Y. Huang, Q. Liu, J. Liu, F. Hu, Z. Pan, Z. Sun, S. Wei, Fast photoelectron transfer in (Cring)-C₃N₄ plane heterostructured nanosheets for overall water splitting, *J. Am. Chem. Soc.* 139 (2017) 3021–3026.
- [19] S. Sun, G. Shen, J. Jiang, W. Mi, X. Liu, L. Pan, X. Zhang, J.J. Zou, Boosting oxygen evolution kinetics by Mn–N–C motifs with tunable spin state for highly efficient solar-driven water splitting, *Adv. Energy Mater.* 9 (2019), 1901505.
- [20] W. Liu, L. Cao, W. Cheng, Y. Cao, X. Liu, W. Zhang, X. Mou, L. Jin, X. Zheng, W. Che, Q. Liu, T. Yao, S. Wei, Single-site active cobalt-based photocatalyst with a long carrier lifetime for spontaneous overall water splitting, *Angew. Chem. Int. Ed.* 56 (2017) 9312–9317.
- [21] D. Zhao, C.L. Dong, B. Wang, C. Chen, Y.C. Huang, Z. Diao, S. Li, L. Guo, S. Shen, Synergy of dopants and defects in graphitic carbon nitride with exceptionally modulated band structures for efficient photocatalytic oxygen evolution, *Adv. Mater.* 31 (2019), e1903545.
- [22] D. Zhao, Y. Wang, C.-L. Dong, Y.-C. Huang, J. Chen, F. Xue, S. Shen, L. Guo, Boron-doped nitrogen-deficient carbon nitride-based Z-scheme heterostructures for photocatalytic overall water splitting, *Nat. Energy* 6 (2021) 388–397.
- [23] F. Yu, T. Huo, Q. Deng, G. Wang, Y. Xia, H. Li, W. Hou, Single-atom cobalt-hydroxyl modification of polymeric carbon nitride for highly enhanced photocatalytic water oxidation: ball milling increased single atom loading, *Chem. Sci.* 13 (2022) 754–762.
- [24] S.K. Sahoo, I.F. Teixeira, A. Naik, J. Heske, D. Cruz, M. Antonietti, A. Savateev, T. D. Kühne, Photocatalytic water splitting reaction catalyzed by ion-exchanged salts of potassium poly(heptazine imide) 2d materials, *J. Phys. Chem. C* 125 (2021) 13749–13758.
- [25] M.A.R. da Silva, I.F. Silva, Q. Xue, B.T.W. Lo, N.V. Tarakina, B.N. Nunes, P. Adler, S.K. Sahoo, D.W. Bahnemann, N. López-Salas, A. Savateev, C. Ribeiro, T.D. Kühne, M. Antonietti, I.F. Teixeira, Sustainable oxidation catalysis supported by light: Fe-poly(heptazine imide) as a heterogeneous single-atom photocatalyst, *Appl. Catal. B* 304 (2022), 120965.
- [26] M.A.R. da Silva, J.C. Gil, N.V. Tarakina, G.T.S.T. Silva, J.B.G. Filho, K. Krambrock, M. Antonietti, C. Ribeiro, I.F. Teixeira, Selective methane photooxidation into methanol under mild conditions promoted by highly dispersed Cu atoms on crystalline carbon nitrides, *Chem. Commun.* 58 (2022) 7419–7422.
- [27] Q. Han, Z. Cheng, B. Wang, H. Zhang, L. Qu, Significant enhancement of visible-light-driven hydrogen evolution by structure regulation of carbon nitrides, *ACS Nano* 12 (2018) 5221–5227.
- [28] J. Fu, J. Yu, C. Jiang, B. Cheng, g-C₃N₄-Based Heterostructured Photocatalysts, *Adv. Energy Mater.* 8 (2018), 1701503.
- [29] C. Han, L. Du, M. Konarova, D.-C. Qi, D.L. Phillips, J. Xu, Beyond hydrogen evolution: solar-driven, water-donating transfer hydrogenation over platinum/carbon nitride, *ACS Catal.* 10 (2020) 9227–9235.
- [30] M. Majdoub, Z. Anfar, A. Ameddous, Emerging chemical functionalization of g-C₃N₄: covalent/noncovalent modifications and applications, *ACS Nano* 14 (2020) 12390–12469.
- [31] S. Yu, J. Li, Y. Zhang, M. Li, F. Dong, T. Zhang, H. Huang, Local spatial charge separation and proton activation induced by surface hydroxylation promoting photocatalytic hydrogen evolution of polymeric carbon nitride, *Nano Energy* 50 (2018) 383–392.
- [32] G. Liu, H. Lv, Y. Zeng, M. Yuan, Q. Meng, Y. Wang, C. Wang, Single-atom Pd–N₃ sites on carbon-deficient g-C₃N₄ for photocatalytic H₂ evolution, *Trans. Tianjin Univ.* 27 (2021) 139–146.
- [33] P. Zhou, Y. Chao, F. Lv, J. Lai, K. Wang, S. Guo, Designing noble metal single-atom-loaded two-dimension photocatalyst for N₂ and CO₂ reduction via anion vacancy engineering, *Sci. Bull.* 65 (2020) 720–725.
- [34] Y. Wang, W. Xu, Y. Zhang, Y. Wu, Z. Wang, L. Fu, F. Bai, B. Zhou, T. Wang, L. Cheng, J. Shi, H. Liu, R. Yang, Introducing spin polarization into atomically thin

- 2D carbon nitride sheets for greatly extended visible-light photocatalytic water splitting, *Nano Energy* 83 (2021), 105783.
- [35] K. Wang, Q. Li, B. Liu, B. Cheng, W. Ho, J. Yu, Sulfur-doped g-C₃N₄ with enhanced photocatalytic CO₂-reduction performance, *Appl. Catal. B* 176–177 (2015) 44–52.
- [36] Y. Li, Y. Wang, C.L. Dong, Y.C. Huang, J. Chen, Z. Zhang, F. Meng, Q. Zhang, Y. Huangfu, D. Zhao, L. Gu, S. Shen, Single-atom nickel terminating sp² and sp³ nitride in polymeric carbon nitride for visible-light photocatalytic overall water splitting, *Chem. Sci.* 12 (2021) 3633–3643.
- [37] G. Kresse, J. Furthmüller, Efficiency of ab-initio total energy calculations for metals and semiconductors using a plane-wave basis set, *Comp. Mater. Sci.* 6 (1996) 15–50.
- [38] G. Kresse, J. Furthmüller, Efficient iterative schemes for ab initio total-energy calculations using a plane-wave basis set, *Phys. Rev. B* 54 (1996) 11169–11186.
- [39] J.P. Perdew, K. Burke, M. Ernzerhof, Generalized gradient approximation made simple, *Phys. Rev. Lett.* 77 (1996) 3865–3868.
- [40] G. Kresse, D. Joubert, From ultrasoft pseudopotentials to the projector augmented-wave method, *Phys. Rev. B* 59 (1999) 1758–1775.
- [41] P.E. Blochl, Projector augmented-wave method, *Phys. Rev. B* 50 (1994) 17953–17979.
- [42] S. Grimme, J. Antony, S. Ehrlich, H. Krieg, A consistent and accurate ab initio parametrization of density functional dispersion correction (DFT-D) for the 94 elements H–Pu, *J. Chem. Phys.* 132 (2010), 154104.
- [43] H. Li, Z. Liang, Q. Deng, M.T. Hu, N. Du, W. Hou, Facile construction of defect-rich rhenium disulfide/graphite carbon nitride heterojunction via electrostatic assembly for fast charge separation and photoactivity enhancement, *ChemCatChem* 11 (2019) 1633–1642.
- [44] X. Zhang, H. Song, C. Sun, C. Chen, F. Han, X. Li, Photocatalytic oxidative desulfurization and denitrogenation of fuels over sodium doped graphitic carbon nitride nanosheets under visible light irradiation, *Mater. Chem. Phys.* 226 (2019) 34–43.
- [45] K. Zhu, C. Chen, H. Xu, Y. Gao, X. Tan, A. Alsaedi, T. Hayat, Cr(VI) Reduction and immobilization by core-double-shell structured magnetic polydopamine@zeolitic idazolate frameworks-8 microspheres, *ACS Sustain. Chem. Eng.* 5 (2017) 6795–6802.
- [46] Y. Zhou, Q. Lu, Q. Liu, H. Yang, J. Liu, J. Zhuang, W. Shi, X. Wang, Architecting hybrid donor–acceptor dendritic nanosheets based on polyoxometalate and porphyrin for high-yield solar water purification, *Adv. Funct. Mater.* 32 (2022), 2112159.
- [47] J. Ekspong, T. Sharifi, A. Shchukarev, A. Klechikov, T. Wågberg, E. Gracia-Espino, Stabilizing active edge sites in semicrystalline molybdenum sulfide by anchorage on nitrogen-doped carbon nanotubes for hydrogen evolution reaction, *Adv. Funct. Mater.* 26 (2016) 6766–6776.
- [48] Y. Li, T. Zhao, M. Lu, Y. Wu, Y. Xie, H. Xu, J. Gao, J. Yao, G. Qian, Q. Zhang, Enhancing oxygen evolution reaction through modulating electronic structure of trimetallic electrocatalysts derived from metal–organic frameworks, *Small* 15 (2019), 1901940.
- [49] H. Li, L. Jian, Y. Chen, G. Wang, J. Lyu, X. Dong, X. Liu, H. Ma, Fabricating Bi₂MoO₆@Co₃O₄ core-shell heterogeneous architectures with Z-scheme for superior photoelectrocatalytic water purification, *Chem. Eng. J.* 427 (2022), 131716.
- [50] B. Kurpil, K. Otte, M. Antonietti, A. Savateev, Photooxidation of N-acylhydrazones to 1,3,4-oxadiazoles catalyzed by heterogeneous visible-light-active carbon nitride semiconductor, *Appl. Catal. B* 228 (2018) 97–102.
- [51] X. Jiang, L. Sun, W. Wang, F. Qin, C. Xie, L. Hu, Y. Zhou, 10 cm² nonfullerene solar cells with efficiency over 10% using HxMoO₃-assisted growth of silver electrodes with a low threshold thickness of 4 nm, *J. Mater. Chem. A* 8 (2020) 69–76.
- [52] C. Cheng, H. Zhang, F. Li, S. Yu, Y. Chen, High performance ammonia gas detection based on TiO₂/WO₃·H₂O heterojunction sensor, *Mater. Chem. Phys.* 273 (2021), 125098.
- [53] J. Cao, W. Nie, L. Huang, Y. Ding, K. Lv, H. Tang, Photocatalytic activation of sulfite by nitrogen vacancy modified graphitic carbon nitride for efficient degradation of carbamazepine, *Appl. Catal. B* 241 (2019) 18–27.
- [54] Q. Deng, G. Ba, T. Huo, H. Li, W. Hou, Atomic carbon chain-linked polymeric carbon nitride: Roles of the carbon chain in enhancing the photocatalytic hydrogen evolution performance, *Appl. Catal. A* 606 (2020), 117833.
- [55] D.L. Yu, J.L. He, Z.Y. Liu, B. Xu, D.C. Li, Y.J. Tian, Phase transformation of melamine at high pressure and temperature, *J. Mater. Sci.* 43 (2008) 689–695.
- [56] C.M. Zhu, A. Gao, Y. Wang, Y. Liu, Pt–Cu bimetallic electrocatalysts with enhanced catalytic properties for oxygen reduction, *Chem. Commun.* 50 (2014) 13889–13892.
- [57] J. Wu, X. Ji, X. Yuan, Z. Zhao, Y. Li, B. Wen, H. Zhang, D. Yu, Y. Zhao, Y. Tian, Regulating polymerization in graphitic carbon nitride to improve photocatalytic activity, *Chem. Mater.* 31 (2019) 9188–9199.
- [58] Z. Liang, X. Zhuang, Z. Tang, H. Li, L. Liu, W. Kang, Soft-template induced synthesis of high-crystalline polymeric carbon nitride with boosted photocatalytic performance, *J. Mater. Chem. A* 9 (2021) 6805–6810.
- [59] Z. Liang, X. Zhuang, Z. Tang, Q. Deng, H. Li, W. Kang, High-crystalline polymeric carbon nitride flake composed porous nanotubes with significantly improved photocatalytic water splitting activity: The optimal balance between crystallinity and surface area, *Chem. Eng. J.* 432 (2022), 134388.
- [60] F. Fina, S.K. Callear, G.M. Carins, J.T.S. Irvine, Structural investigation of graphitic carbon nitride via XRD and neutron diffraction, *Chem. Mater.* 27 (2015) 2612–2618.
- [61] Y. Wang, X. Liu, J. Liu, B. Han, X. Hu, F. Yang, Z. Xu, Y. Li, S. Jia, Z. Li, Y. Zhao, Carbon quantum dot implanted graphite carbon nitride nanotubes: excellent charge separation and enhanced photocatalytic hydrogen evolution, *Angew. Chem. Int. Ed.* 57 (2018) 5765–5771.
- [62] C. Lv, Y. Qian, C. Yan, Y. Ding, Y. Liu, G. Chen, G. Yu, Defect engineering metal-free polymeric carbon nitride electrocatalyst for effective nitrogen fixation under ambient conditions, *Angew. Chem. Int. Ed.* 57 (2018) 10246–10250.
- [63] H. Lei, M. Wu, F. Mo, S. Ji, X. Dong, Y. Jia, F. Wang, Z. Wu, Efficiently harvesting the ultrasonic vibration energy of two-dimensional graphitic carbon nitride for piezocatalytic degradation of dichlorophenols, *Environ. Sci. Nano* 8 (2021) 1398–1407.
- [64] T. Huo, Q. Deng, F. Yu, G. Wang, Y. Xia, H. Li, W. Hou, Ion-induced synthesis of crystalline carbon nitride ultrathin nanosheets from mesoporous melon for efficient photocatalytic hydrogen evolution with synchronous highly selective oxidation of benzyl alcohol, *ACS Appl. Mater. Interfaces* 14 (2022) 13419–13430.
- [65] P. Wang, L. Tian, X. Gao, Y. Xu, P. Yang, Two-photon absorption in a defect-engineered carbon nitride polymer drives red-light photocatalysis, *ChemCatChem* 12 (2020) 4185–4197.
- [66] J. Wu, N. Li, H.-B. Fang, X. Li, Y.-Z. Zheng, X. Tao, Nitrogen vacancies modified graphitic carbon nitride: Scalable and one-step fabrication with efficient visible-light-driven hydrogen evolution, *Chem. Eng. J.* 358 (2019) 20–29.
- [67] X. Li, P. Cui, W. Zhong, J. Li, X. Wang, Z. Wang, J. Jiang, Graphitic carbon nitride supported single-atom catalysts for efficient oxygen evolution reaction, *Chem. Commun.* 52 (2016) 13233–13236.
- [68] G. Ba, T. Huo, Q. Deng, H. Li, W. Hou, Mechanochemical synthesis of nitrogen-deficient mesopore-rich polymeric carbon nitride with highly enhanced photocatalytic performance, *ACS Sustain. Chem. Eng.* 8 (2020) 18606–18615.
- [69] H. Li, C. Jin, Z. Wang, Y. Liu, P. Wang, Z. Zheng, M.-H. Whangbo, L. Kou, Y. Li, Y. Dai, B. Huang, Effect of the intra- and inter-triazine N-vacancies on the photocatalytic hydrogen evolution of graphitic carbon nitride, *Chem. Eng. J.* 369 (2019) 263–271.
- [70] K.L. Corp, C.W. Schlenker, Ultrafast spectroscopy reveals electron-transfer cascade that improves hydrogen evolution with carbon nitride photocatalysts, *J. Am. Chem. Soc.* 139 (2017) 7904–7912.
- [71] L. Jing, R. Zhu, D.L. Phillips, J.C. Yu, Effective prevention of charge trapping in graphitic carbon nitride with nanosized red phosphorus modification for superior photo(electro)catalysis, *Adv. Funct. Mater.* 27 (2017), 1703484.
- [72] S. Megala, P. Ravi, P. Maadeswaran, M. Navaneethan, M. Sathish, R. Ramesh, The construction of a dual direct Z-scheme NiAl LDH/g-C₃N₄/Ag₃PO₄ nanocomposite for enhanced photocatalytic oxygen and hydrogen evolution, *Nanoscale Adv.* 3 (2021) 2075–2088.
- [73] X. Cheng, Y. Li, L. Zheng, Y. Yan, Y. Zhang, G. Chen, S. Sun, J. Zhang, Highly active, stable oxidized platinum clusters as electrocatalysts for the hydrogen evolution reaction, *Energy Environ. Sci.* 10 (2017) 2450–2458.
- [74] Z. Ma, C. Chen, X. Cui, L. Zeng, L. Wang, W. Jiang, J. Shi, Hydrogen evolution/oxidation electrocatalysts by the self-activation of amorphous platinum, *ACS Appl. Mater. Interfaces* 13 (2021) 44224–44233.
- [75] P. Li, X.Y. Chen, H.C. He, X. Zhou, Y. Zhou, Z.G. Zou, Polyhedral 30-faceted BiVO₄ microcrystals predominantly enclosed by high-index planes promoting photocatalytic water-splitting activity, *Adv. Mater.* 30 (2018), 1703119.
- [76] S.Y. Wang, Y.Y. Gao, S. Miao, T.F. Liu, L.C. Mu, R.G. Li, F.T. Fan, C. Li, Positioning the water oxidation reaction sites in plasmonic photocatalysts, *J. Am. Chem. Soc.* 139 (2017) 11771–11778.